Desalination and Water Treatment
www.deswater.com

doi: 10.5004/dwt.2021.27274

226 (2021) 431–440
June

Sm-Co substituted M-type lead hexaferrite for dielectric properties and visible light driven methylene blue degradation in industrial wastewater

Muhammad Jamshaid[a], Muhammad Imran Khan[b], Hasan M. Khan[c], Abdul Rauf[a], Ome Parkash Kumar[a], Muhammad Nadeem Akhtar[a], Shahid Iqbal[a], Abdallah Shanableh[b], Aziz ur Rehman[a,*]

[a]*Institute of Chemistry, Baghdad-ul-Jadeed Campus, The Islamia University of Bahawalpur, Bahawalpur 63100, Pakistan, emails: azizypk@yahoo.com (A. ur Rehman), jimmichemist@gmail.com (M. Jamshaid), abdul.rauf@iub.edu.pk (A. Rauf), okumar112@gmail.com (O. Parkash Kumar), nadeemchem@yahoo.com (M.N. Akhtar), shahidiqbal0102@gmail.com (S. Iqbal)*
[b]*Research Institute of Sciences and Engineering, University of Sharjah, Sharjah, 27272, United Arab Emirates, email: raoimranishaq@gmail.com (M. Imran Khan), shanableh@sharjah.ac.ae (A. Shanableh)*
[c]*Institute of Physics, Baghdad-ul-Jadeed Campus, The Islamia University of Bahawalpur, Bahawalpur 63100, Pakistan, email: hmkhan@iub.edu.pk*

Received 20 November 2020; Accepted 28 March 2021

ABSTRACT

The rapid industrialization of the world is critically influencing our environment and natural ecosystem. The researchers are taking keen interest to invent novel material as photocatalyst for non-degradable organic pollutants. Herein, we have fabricated Sm and Co substituted M-type hexaferrite with composition $Ca_{0.5}Pb_{0.5-x}Sm_xCo_yFe_{12-y}O_{19}$, ($x$ = 0.00–0.1; y = 0.00–1.00) by sol–gel auto-combustion approach. The effect of Sm^{2+} and Co^{3+} substitution in calcium-lead hexaferrite has been investigated for structural, morphological, dielectric and photocatalytic applications for organic pollutants. X-ray diffraction study exhibited the presence of the single-phase M-type hexaferrite with size ranged between 19–23 nm. The particle size, shape and elemental composition were determined by scanning electron microscopy and energy-dispersive X-ray spectroscopy analysis. It was investigated that the electrical resistivity was decreased, and drifts mobility increased with increasing Sm^{2+} and Co^{3+} contents in the doped materials. An inverse relation has been established between the dielectric constant and the dielectric loss up to a frequency of 9.0 GHz and remains constant above this frequency range. The synthesized materials may prove a suitable contender in the domain of high-frequency devices like circulators, filters, transformers and antennas and environmental remediation. The energy bandgap (E_g) was calculated from UV-visible absorbance spectra by Tauc plot. It showed decreasing trend from 2.2 to 1.95 eV for precursor and doped material ($Ca_{0.5}Pb_{0.5-x}Sm_xCo_yFe_{12-y}O_{19}$, x = 0.1; y = 1.00) respectively. Narrowing of bandgap is considered an important factor for the degradation of industrial effluents. The doped materials have also been explored to study the photocatalytic efficiency using a batch reactor to remove methylene blue dye from the textile synthetic wastewater in the presence of visible light radiations at 668 nm, recording 87.50% of degradation efficiency.

Keywords: Dielectric constant; Dielectric loss; Dye degradation; Hexaferrite; Resistivity

* Corresponding author.

1. Introduction

Hexagonal ferrites, well-known as hexaferrites were discovered in 1950 [1]. Due to their unique magnetic and electrical behavior, hexagonal hexaferrites have drawn keen interest due to their enormous applications [2]. In a particular, these materials were endowed with low dielectric constant, high electrical resistivity, enhanced magnetization capacity, outstanding decomposition resistivity, chemical constancy and high coerciveness; such characteristics are valued in microwave and radio frequency material [3]. They have established a rising role in the renovation of high-quality circulators, filters, transformers and antennas [4]. These benign characteristics are generally ascribed to the shape, particle size and preparation methods. Although, strontium ($SrFe_{12}O_{19}$) and barium ($BaFe_{12}O_{19}$) hexaferrites are being paid copious attention owing to their functionality but recently, research is mostly being focused towards lead hexaferrites [5].

As lead hexaferrites possess the lower crystallization temperature compared to pristine barium and strontium hexaferrite [6]. Noteworthy, the structural aspect of lead-hexaferrite ($PbFe_{12}O_{19}$) is least explored and hence needs meticulous exploration. It has been reported earlier [7] that rare earth metals doping in M-type hexaferrite reduces the porosity as well as a non-magnetic phase which consequently enhances the coercivity. Therefore, Sm was used as a dopant. Co is non-toxic and has high electrical properties. Therefore, it can preferably be used for dielectric and photocatalytic activities (degradation power). Because of this, we have selected Sm and Co as dopants in our current work.

Various methods are practiced for the synthesis of hexaferrite, among these ammonia nitrate melt [8], co-precipitation process [9], micro-emulsion [10], sol–gel and hydrothermal are well-recognized [11]. The sol–gel is regarded as better as it involves exothermic and self-sustaining anionic redox reaction of xerogel. Xerogel is formed from an aqueous solution containing desired metal salts solutions (oxidizer) and organic complexant (reductant) [12]. Evaluation of gases during the combustion of xerogel favours the formation of hexaferrite nanopowder and avoids agglomeration [13]. The advantages of the sol–gel auto combustion method include high product purity, good chemical homogeneity, narrow particle size distribution, simple equipment and preparation process [14]. The electric, magnetic, structural, energy proficiency, the shorter reaction time, clear crystalline product, are the properties of M-type Pb hexaferrite that depend upon the substitutions of Pb^{2+} and Fe^{3+} ions with Sm^{2+} and Co^{3+} cations [15]. The substantial role of calcium content in the ferrite is to control the particle size up to the required limit. M-type Pb hexaferrite doped with Sm and Co has not been explored to the best of our knowledge.

The introduction of rare earth elements (RE) in calcium-lead M-type hexaferrite cause a reduction in non-magnetic character and porosity, the enhancement in resistivity and saturation magnetism [16]. Notably, the room temperature resistivity of M-type Pb hexaferrite doped with Sm and Co ions has been determined. Dyes are complex non-degradable organic compounds that enter the environment by dyeing and completion in the textile industry [17].

Studies have shown that textile wastewater has low biochemical oxygen demand/chemical oxygen demand (0.1) which was resulted from the non-biodegradability of dyes [18]. The extensive release of dyes into water leads to serious toxicity for the living organism and damage to the environment [19]. Commonly used dye removing techniques have many limitations like low removal efficiency, high cost, selectivity and secondary pollutant formation. Therefore, a low cost, versatile, broad spectrum and environmental friendly technique like photocatalysis was considered necessary [20–22].

Methylene blue is a cationic aromatic compound containing sulphur used as a dye in the textile industry [23]. Sm-Co calcium lead hexaferrite was investigated for degradation of methylene blue from textile synthetic wastewater in the presence of visible light radiations. The most degradation reactions of toxic organic pollutants took place in the visible light. Hence, the sunlight was preferred to develop photocatalyst to degrade a pollutant. The calculated bandgaps of the precursor and the doped materials are manifested in the visible region (1.95–2.2 eV) accordingly. Materials were believed to be active for the degradation of methylene blue. The aim of this research is to explore the dielectric properties and photocatalytic application in removing the methylene blue (MB) from textile wastewater of the prepared nanomaterial. These materials may find applications in the environmental remediation and high-frequency devices domains.

2. Experimental

2.1. Materials

Analytical grade iron chloride ($FeCl_3{\cdot}6H_2O$), citric acid ($C_6H_8O_7$), cobalt chloride ($CoCl_3$), calcium chloride ($CaCl_2$), samarium oxide (Sm_2O_3), methylene blue, lead nitrate $Pb(NO_3)_2$, nitric acid and ammonia solution (NH_3) were obtained from Merck KGaA (Germany). Deionized water was used throughout the work.

2.2. Sm-Co substituted calcium-lead ferrite nanomaterials

Samples with composition of $Ca_{0.5}Pb_{0.5-x}Sm_xCo_yFe_{12-y}O_{19}$, ($x$ = 0.00–0.1; y = 0.00–1.00) were prepared by sol–gel auto-combustion method as reported in literature [24]. The metal salts/oxides were dissolved by stirring in deionized water at 85°C for 30 min. The pH of the solution was maintained at 8.0 by the addition of 3.0 M ammonia solution, as in alkaline solution, sufficient no of OH^- ions are produced which assist photodegradation process, followed by evaporation of mixture at 80°C to obtain gel for 6 h. The temperature of the gel was increased up to 200°C and burned to brownish-black powder. Finally, the powder was calcinated at 1,000°C for 12 h, subsequently grounded to get a fine powder.

2.3. Photocatalytic degradation

Photocatalytic potential for the degradation of methylene blue dye solution was evaluated by using prepared samples. The time for the experiment was set between 10 AM to 3 PM due to the least fluctuations in the light intensity in May (Pakistan Standard Time) [25]. For the

determination of the effect of pH change, the dye solutions of pH 4, 7.3 and 11 were used. The pH of the solution was adjusted by the use of 0.5 M HCl or NaOH solutions. The experiment was carried out in a 100 mL glass beaker under the specific conditions accordingly. A 20 mL of the dye solution was stirred for 120 min in the presence of visible light and in the absence of a photocatalyst [22]. No appreciable change in the concentration of MB dye solution was noted within the specified time interval. The maximum wavelength (λ_{max}) for the absorbance of MB dye solution is 668 nm [21]. The decreased intensity of MB dye solution was noted for the determination of the degradation process. First, the dye solution and the photocatalyst were put under the dark condition and stirred continuously for 30 min to establish equilibrium. The amount of the photocatalyst used was 1.5 g/L. After the specified interval of the time, the reaction mixture was centrifuged, filtered and subsequently analyzed with UV-visible a spectrophotometer for a zap of methylene blue (MB) dye solution concentration.

2.4. Characterization

Structural properties of the prepared samples like average crystallite size (D), lattice parameters (a and c), unit cell volume (V_{cell}) and X-ray density were analyzed by JEOL X-ray diffraction meter fortified with CuKa radiations (wavelength = 1.5418 Å). While, energy-dispersive X-ray spectroscopy (EDX) spectra of samples were obtained using INCA 100/Oxford UK, JEM-2100). The morphological analysis of the selected doped materials was affirmed by a scanning electron microscope (JEOL, Japan JSM5910). The resistivity was measured by using a two probe method source meter (model 2400). The electrical properties of samples were investigated by using LCR meter (model 8101 Gw, Taiwan). On the other hand, the UV-Visible spectrophotometer (CeCil CE 7400, Waltham, MA, USA) was used to record the absorbance of the dye solutions.

3. Results and discussion

3.1. EDX analysis

Fig. 1 illustrates the presence of Pb, Fe, Ca, Co, Sm and O in the samples of doped materials. It manifests the purity and composition of the doped samples which also depicts the approximate composition of elements by weight percentage present in the doped nanomaterial. Furthermore, it also reveals that Pb^{2+} and Fe^{3+} were substituted by stoichiometric amounts of Co^{3+} and Sm^{2+} in doped hexaferrite [26].

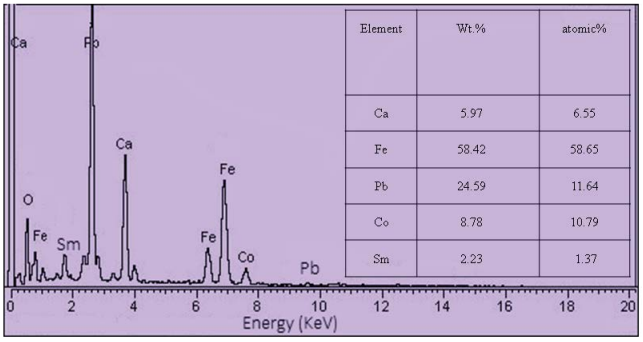

Element	Wt.%	atomic%
Ca	5.97	6.55
Fe	58.42	58.65
Pb	24.59	11.64
Co	8.78	10.79
Sm	2.23	1.37

Fig. 1. EDX analysis of M-type hexaferrites $Ca_{0.5}Pb_{0.40}Sm_{0.1}Co_{1.0}Fe_{11.90}O_{19}$.

3.2. X-ray diffraction analysis

X-ray diffraction (XRD) analysis of the $Ca_{0.5}Pb_{0.5-x}Sm_xCo_yFe_{12-y}O_{19}$ (x = 0.00–0.1 and y = 0.00–1.00) nanomaterial are presented in Fig. 2. From X-ray diffraction patterns, it has been inferred that the samples correspond to the standard pattern (ICDD 00-051-1879) [27]. Besides, it also shows that the peak intensity was increased by increasing the content of dopants into samples of doped materials. The parameters such as unit cell volume (V_{cell}), cell constant (a and c) and crystallite size have also been derived from XRD data. The difference in ionic radius between Pb^{2+} (0.739 Å) and Fe^{3+} (0.641 Å) is attributed to the increase in lattice constants [28]. Bulk density was calculated from XRD data by using the following formula:

$$d_{bulk} = \frac{m}{\pi r^2 h} \quad (1)$$

where r describes pellet radius, m presents pellet mass, and h stands for pellet thickness. It has been established that the doped samples possess a higher bulk density (2.51–2.94 g/cm^3) compared to pristine materials as listed in Table 1. This enhancement in the bulk density is specifically ascribed to the substitution of Sm^{3+} (7.54 g/cm^3) with Fe^{2+} ions (2.55 g/cm^3).

The average crystallite size (D) has been estimated by employing Debye–Scherrer:

$$D = \frac{K\lambda}{\beta}\cos\theta_B \quad (2)$$

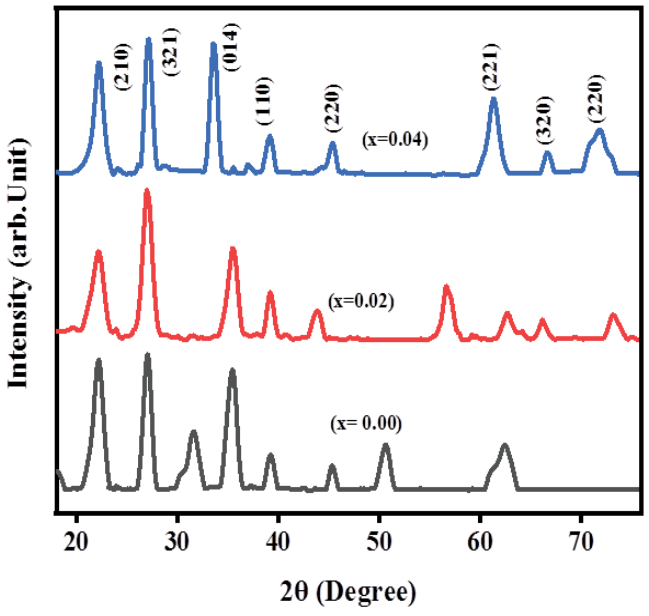

Fig. 2. XRD analysis of M-type hexaferrite $CaPbSmCoFe_{12}O_{19}$.

where K (0.89) shows the shape constant of the hexagonal system, β denotes full-width half maxima (FHWM), and θ_B is Bragg's angle of diffraction. The average crystallite size is found to range between 19–23 nm in the doped samples. The crystallite size <50 is necessary for obtaining the appropriate signal to noise ratio, as materials within this dimension may be used in the high density recording media [29]. The cell volume was recorded ranging between 49.75–139 Å for the doped materials. This parameter was calculated by using the given relation:

$$\text{Cell volume} = \left(a^2 \times c\right) \tag{3}$$

where a and c are lattice parameters of particles.

X-ray density has been determined by using the below expression:

$$\rho_x = \frac{Z_x M}{N_A X V_{\text{cell}}} \tag{4}$$

where M denotes molecular mass and Z shows the orthorhombic system of material.

3.3. Lattice parameters

Figs. 3a and b demonstrate the lattice parameter variations in $Ca_{0.5}Pb_{0.5-x}Sm_xCo_yFe_{12-y}O_{19}$ (x = 0.00–0.1; y = 0.00–1.00). These parameters were derived from X-ray diffraction data. The calculated values of the lattice parameters a and c ranged between a = (2.62–3.73 Å) and c = (4.79–6.58 Å), respectively. The trend of increasing lattice parameters was connected to the substitution of Sm (x = 0.00–0.1) RE metal, which in turn results in a multitude of ionic species and a larger radius compared to the host metal ions [30]. Besides, the enhancement in dielectric constant and dielectric loss was attributed to the substitution of Sm and Co within the pristine host metal oxides. The enhanced lattice parameter was associated with interatomic distance. As the content Sm was increased within the doped sample, interionic distance was also increased due to the larger RE ionic radius compared to the host metals [31].

3.4. Scanning electron microscope analysis

Morphology and the microstructure of the synthesized materials $Ca_{0.5}Pb_{0.5-x}Sm_xCo_yFe_{12-y}O_{19}$ were analyzed by scanning electron microscopy and attained results are shown in Fig. 4. The doped nanomaterial was nearly of spherical shape. Besides, these were distributed uniformly and such type of morphology was considered suitable for the microwave absorption and recording devices. From here, it can be deduced that smaller lead content into the sample results in formation of the smaller grain sized particles. Contrarily, the increase in Pb content within the doped nanomaterial results in the large grain sized articles. Although, increased quantity of lead improves the magnetic moment of the crystalline structure as it modifies the super-exchange coupling between iron cations.

3.5. Dielectric properties

3.5.1. Dielectric constant

The dielectric constant and the dielectric loss provide insight into the electrical behavior of the charge carrier vs. frequency is plotted as shown in Fig. 5a. Noteworthy, dielectric constant values were decreased for the first three samples with the increase of frequency due to the interfacial polarization. Further, no appreciable change recorded in dielectric constants in the remaining

Table 1
Lattice parameters of $CaPbSmCoFe_{12}O_{19}$ M-type hexaferrites

Compositional formula	A	C	c/a	V_{cell} (Å)	d_b (g/cm³)
$Ca_{0.5}Pb_{0.5}Fe_{12}O_{19}$	2.62	4.79	1.82	49.75	2.51
$Ca_{0.5}Pb_{0.48}Sm_{0.02}Co_{0.2}Fe_{11.98}O_{19}$	2.78	4.97	1.79	49.77	3.30
$Ca_{0.5}Pb_{0.46}Sm_{0.04}Co_{0.4}Fe_{11.96}O_{19}$	3.20	5.60	1.75	151	3.29
$Ca_{0.5}Pb_{0.44}Sm_{0.06}Co_{0.6}Fe_{11.94}O_{19}$	3.28	5.80	1.77	141	2.95
$Ca_{0.5}Pb_{0.42}Sm_{0.08}Co_{0.8}Fe_{11.92}O_{19}$	3.71	6.50	1.75	140	2.94
$Ca_{0.5}Pb_{0.40}Sm_{0.1}Co_{1.00}Fe_{11.90}O_{19}$	3.73	6.58	1.76	139	2.94

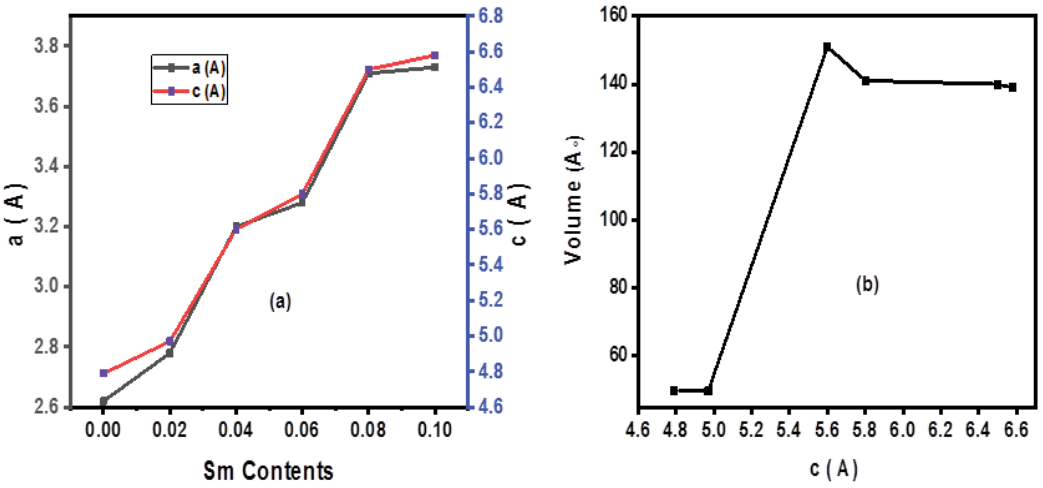

Fig. 3. (a and b) Lattice parameter of $Ca_{0.5}Pb_{0.5-x}Sm_xCo_yFe_{12-y}O_{19}$ (x = 0.00–0.1; y = 0.00–1.00).

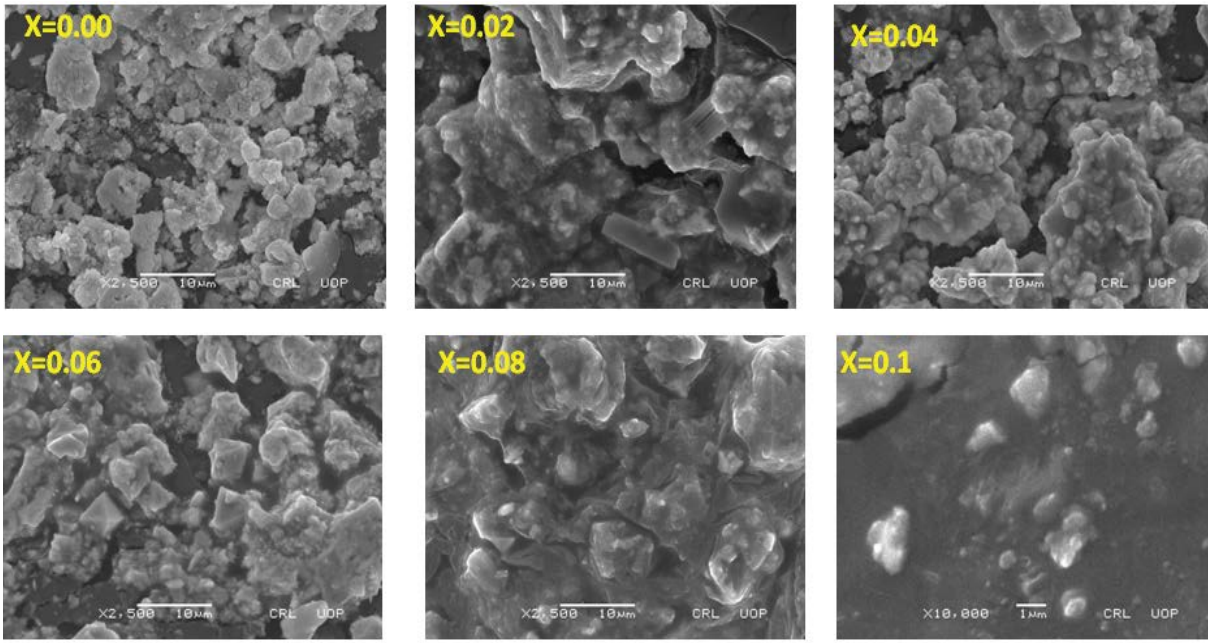

Fig. 4. Scanning electron microscopy images of different magnification of the Sm-Co doped M-type Ca-Pb hexaferrites.

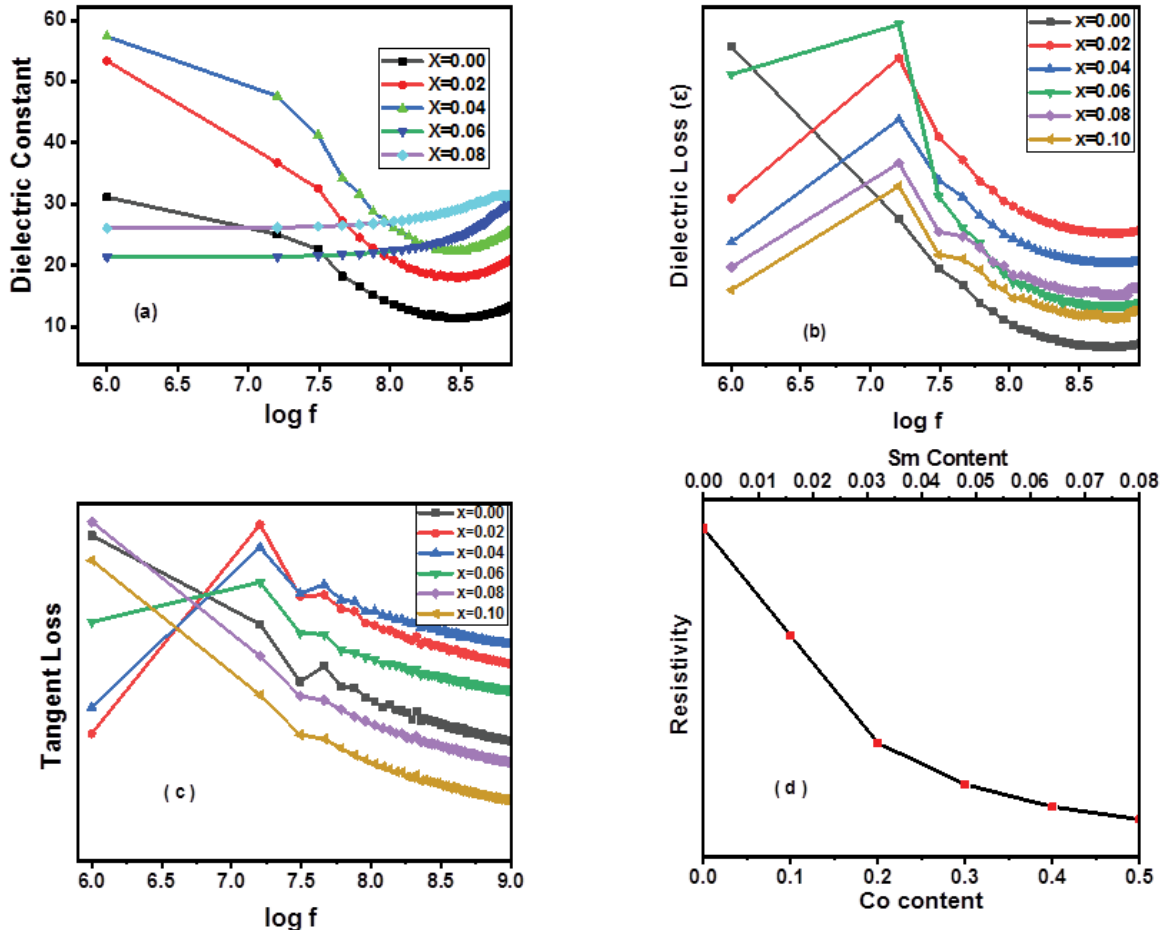

Fig. 5. (a–c) Dielectric constant, dielectric loss, tangent loss vs. log*f* for $Ca_{0.5}Pb_{0.5-x}Sm_xCo_yFe_{12-y}O_{19}$, ($x$ = 0.00–0.1; y = 0.00–1.00) and (d) resistivity vs. metal content.

two compositions compared to the previous samples; dielectric constant values became constant even at the higher frequency. It manifested usual behavior regarding hexaferrite following Maxwell–Wagner and Koop's theory [32]. Keeping in the view above mentioned attributes, the dielectric constants of heterogeneous nanomaterials are considered the most important because of being composed of a double layer with well-conducting grains separated by poorly conducting grain boundaries [33]. For the doped material ($Ca_{0.5}Pb_{0.5-x}Sm_xCo_yFe_{12-y}O_{19}$), at a low-frequency surface charge polarization is created on grain boundaries. Free charge and polarization of the grain boundaries manage surface charge polarization phenomena. The charge polarization was largely dependent upon the concentration of Fe^{2+} in ferrites [34]. On the other hand, Co^{3+} ions demonstrated the tendency of penetration into the tetrahedral site, thus resulting into a probable reduction in Fe^{2+} ions concentration at the tetrahedral site. Subsequently, electric polarization and dielectric constant are reduced by further addition of Sm^{2+} ions within the ferrites. Sm^{2+} ions do not boost the conduction process but in reality, obstruct the movement of charge carriers. Koop suggested that dielectric constant values are related to the applied frequency and grain boundaries of sample material. The dielectric constants obtained from Sm and Co substitution of Pb hexaferrite were much smaller due to the creation of high density defect within the host material therein. From these results, it is clear that Sm and Co substituted Pb hexaferrite was a much better dielectric nanomaterial and suitable for application in high-frequency devices.

3.5.2. Dielectric loss

Figs. 5b and c show curves of dielectric loss and tangent loss under the function of frequency for $Ca_{0.5}Pb_{0.5-x}Sm_xCo_yFe_{12-y}O_{19}$, ($x$ = 0.00–0.1; y = 0.00–1.00). The dielectric tangent loss describes the energy dissipation in the doped sample used as dielectric media. It has also been established that the lowered dielectric loss is an indication of the low core loss and the high frequency. In $Ca_{0.5}Pb_{0.5-x}Sm_xCo_yFe_{12-y}O_{19}$, the dielectric loss was significant at the high frequency. It was ascribed to the increase in Sm^{2+} and Co^{3+} content while the decrease in Fe^{3+} because of reduction to Fe^{2+} ions, which were responsible for conduction losses. As electron exchange between Fe^{3+} and Fe^{2+} ions required a lower amount of energy, it favours a drop in dielectric loss [35]. It has been observed that energy loss was higher in the low-frequency region and reportedly lower in the high-frequency region. In general, lead poses greater resistance in contrast to iron at 300 K, which increases the specific strength of lead. Thus the resistance of lead in addition to the effect of Sm and Co dopants results to decrease in the dielectric parameters.

3.5.3. Room temperature resistivity

The resistivity curve as a function of the amount of Sm and Co contents can be seen in Fig. 5d. In Sm and Co substituted Ca-Pb hexaferrite, the decrease in the resistivity was noticed. This decrease in resistivity is ascribed to the formation of Fe^{2+} ions from Fe^{3+} by super exchange interaction of the octahedral to the tetrahedral site [36]. A distinct decrease in the resistivity was recorded between 6.64×10^8 Ω cm to 4.85×10^5 Ω cm. The main cause of decreased resistivity is associated with the addition of Sm^{2+} and Co^{3+} ions in the host material.

3.6. Determination of bandgap

The spectra (Fig. 6b) demonstrate the energy of forbidden bands; both precursor and product are within the visible light spectral region. The calculated bandgaps values were 2.2 and 1.95 eV for the precursor and product, respectively. For proper functioning of the photocatalyst under the visible light, pertinent bandgap energy is prerequisite. In certain cases, any impurity or dopant is required to manipulate the bandgap energy of the pristine (pure) materials for the optimization of bandgap energies. So, doping of Sm and Co raised structural defects within the

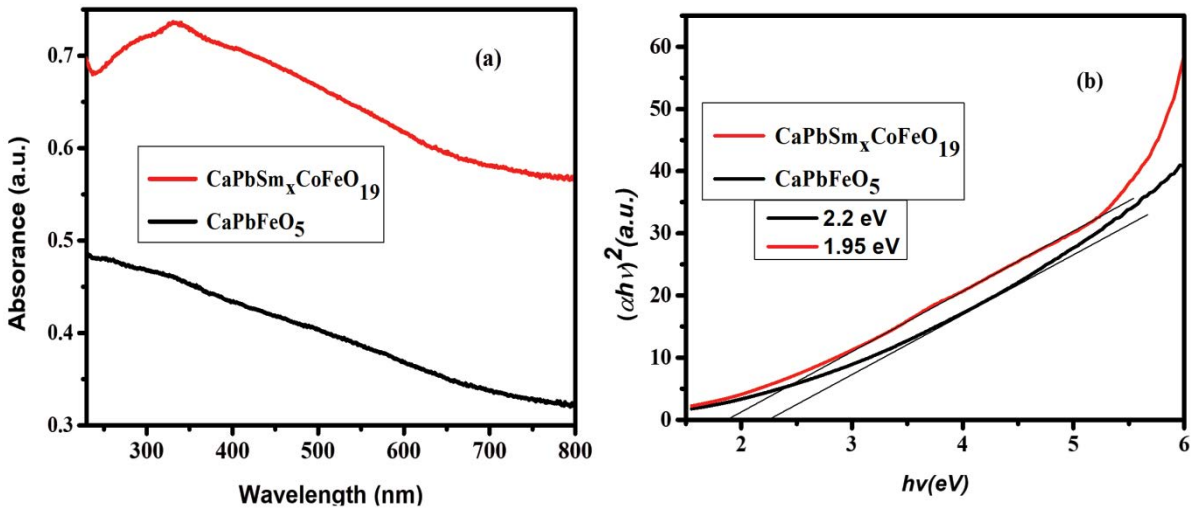

Fig. 6. (a) UV-Visible spectra of sample ($Ca_{0.5}Pb_{0.5-x}Sm_xCo_yFe_{12-y}O_{19}$, x = 0.04; y = 0.4) and precursor ($Ca_{0.5}Pb_{0.5}Fe_{12}O_{19}$, x = 0.00; y = 0.00) and (b) Tauc plots of sample and precursor for bandgap determination.

lead hexaferrite pristine material by increasing the number of oxygen vacancies in the composite. It was observed that the bandgap energies for the doped materials are lower than pure hexaferrites, which may be attributed to the decrease in vacancy between the conduction band and valance band resulting from energy states that inhibit the electron–hole recombination [37–39]. These bandgaps revealed the higher photolytic activity of organic pollutants such as MB.

3.7. Photocatalytic performance

From the photodegradation experiments, the photocatalyst $Ca_{0.5}Pb_{0.5-x}Sm_xCo_yFe_{12-y}O_{19}$, x = 0.04, y = 0.4 was found most effective for the degradation of methylene blue solution under the solar light irradiation. The removal efficiency of methylene blue dye was calculated by using the following relation [40].

$$\%\text{Removal} = \frac{C}{C_0} \times 100 \tag{5}$$

where C_0 is the initial concentration of MB dye, C is the concentration of dye at a certain time interval. The photocatalyst showed 87.50% degradation efficiency for methylene blue. The enhanced photocatalytic performance of the Ca-Pb M-type hexaferrite is attributed to more energy sites and efficient charge transfer due to the substitution of samarium and cobalt [41,42]. From the results, the decrease in the concentration is indicated with the time interval.

3.7.1. Effect of contact time on the photodegradation

The contact time is a crucial parameter for the degradation of methylene blue over the surface of the photocatalyst $Ca_{0.5}Pb_{0.5-x}Sm_xCo_yFe_{12-y}O_{19}$, ($x$ = 0.04; y = 0.4). The contact time corresponds to the duration of the degradation of the dye on the surface of the photocatalyst. Fig. 6b depicts the effect of the contact time for the degradation of methylene blue. It was found that the efficiency of the dye degradation was increased with increasing the contact time and the concentration of the dye decreased with the increasing contact time as shown in Fig. 7a. Furthermore, the rate of degradation decreases with the passage of the time. In the dark phase of 30 min, only 42% of the dye degradation was recorded. However, in 120 min 87.50% of the dye degraded and after this time interval no noticeable decrease in concentration was noticed.

3.7.2. Effect of photocatalyst dosage on the photodegradation

Generally, the photocatalytic degradation efficiency was increased with the photocatalyst dosage up to a certain amount. Herein, the amount of the photocatalyst has been optimized at 1.5 g/L as maximum photocatalytic degradation of MB was recorded. However, in the absence of the photocatalyst no appreciable has been reported.

3.7.3. Kinetic studies

The kinetic study was carried out to find the rate and to certain extent determine the mechanism of the photodegradation. For this purpose, pseudo-first-order was fitted in for Langmuir–Hinshelwood model; the expression is given as follows [43]:

$$\ln\frac{C_t}{C_0} = -kt \tag{6}$$

The rate of dye degradation was carried out by plotting graph between C/C_0 vs. time as demonstrated in Fig. 7e. From the results of Fig. 7e, the correlation constants values obtained were 0.970, 0.990 and 0.977 (Table 2) strongly support the pseudo-first-order for the degradation of methylene blue. The pseudo-first-order rate constants for $CaPbSmCoFeO_{19}$ photocatalyst of the degradation of methylene blue dye were 0.00564, 0.00354 and 0.00341, respectively. These results suggest efficient photo-degradation performance for MB.

3.7.4. Mechanism of the dye degradation

In the case of the degradation of dyes, the electrons are generated by absorption of visible light in the valence band (VB) of the photocatalyst. The photocatalyst generated various active species for crucial for the degradation of dye. Fig. 8 depicts a general mechanism and generation of attacking radicals for the degradation of methylene blue molecules. The electrons are then promoted to the conduction band (CB) of the photocatalyst and finally embark upon the surface of the photocatalyst. Oxygen present in the aqueous environment of the dye solution is attacked by electron and superoxide radicals (O_2^-) were produced. These O_2^- radicals may interact with the water molecule to form H_2O. With great ease H_2O turns into more stable radical, OH. At least, two radicals may attack MB dye. It was interpreted that both OH and O_2^- were generally involved in the degradation of MB. The general mechanism for the degradation of MB dye was described as in following relation [35,36].

$$CaPbSmCoFeO_{19} + h\nu \rightarrow h^+ + e^- \tag{7}$$

$$O_2 + e^- \rightarrow O_2^- \tag{8}$$

$$H_2O + O_2^- \rightarrow HO_2 + {}^-OH \tag{9}$$

$$O_2 + e^- \rightarrow O_2^- \tag{10}$$

$$O_2^{\bullet} + H_2O_2 \rightarrow {}^{\bullet}OH + {}^-OH \tag{11}$$

$$O_2^{\bullet} + {}^{\bullet}OH + MB \rightarrow \text{Oxidation products} \tag{12}$$

4. Conclusions

In summary, M-type hexaferrites with the chemical composition of $Ca_{0.5}Pb_{0.5-x}Sm_xCo_yFe_{12-y}O_{19}$ (x = 0.00–0.1; y = 0.00–1.00) were successfully synthesized via sol–gel auto combustion method to obtain a single plumbite phase with an average crystallite size ranging between 19–23 nm. Dielectric constant and loss follow usual dispersion behavior in accordance with Koop's and Maxwell–Wagner

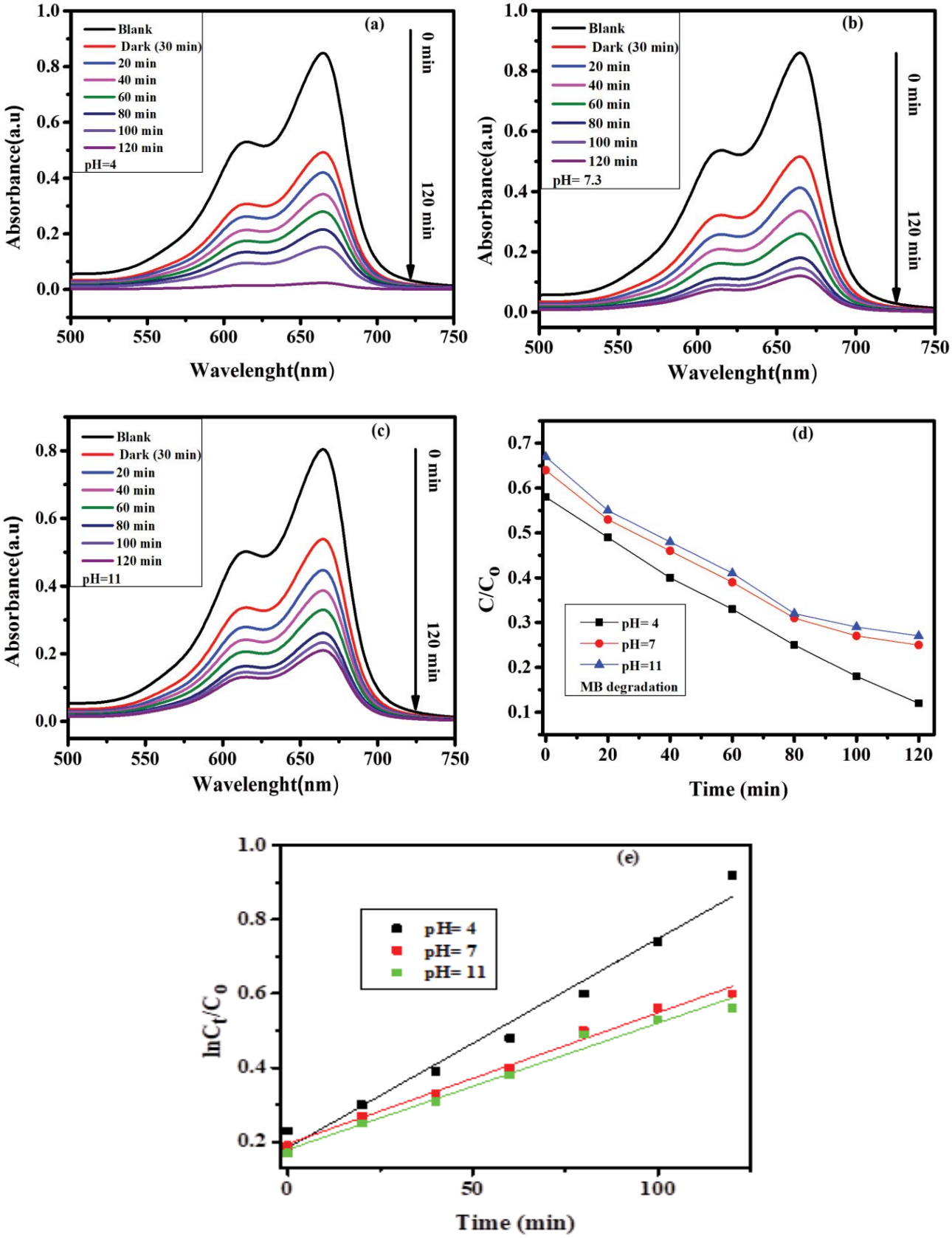

Fig. 7. (a–c) Photocatalytic degradation of methylene blue (MB) at pH: 4, 7.3 and 11, respectively, (d) rate of degradation of methylene blue at pH: 4, 7.3 and 11, and (e) kinetic studies of methylene blue.

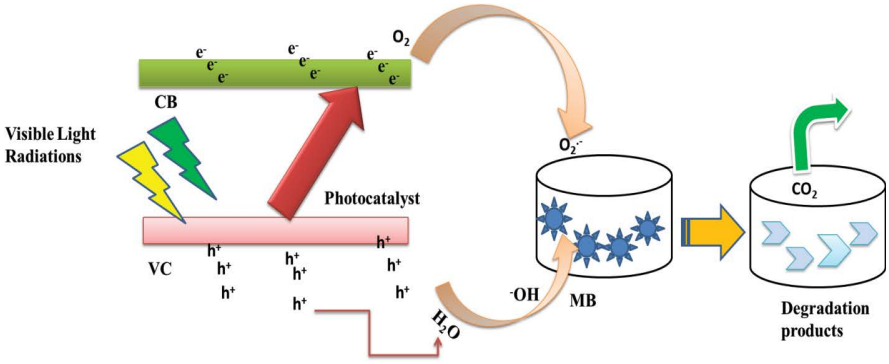

Fig. 8. General mechanism of the photodegradation of MB dye.

Table 2
Pseudo-first-order kinetics results of MB degradation

Photocatalyst (g/L)	Dye MB (mg/L)	Initial pH	k (min^{-1})	R^2
1.5	10	4	0.00564	0.970
1.5	10	7	0.00354	0.990
1.5	10	11	0.00341	0.977

theories, two-layer models. The $Ca_{0.5}Pb_{0.5-x}Sm_xCo_yFe_{12-y}O_{19}$ (x = 0.00–0.1; y = 0.00–1.00) hexaferrite materials exhibited semiconductor behavior, resistivity drop (11.51 Ω cm) was observed with a rise in temperature. Furthermore, the drift mobility was increased with increasing temperature due to thermal activation of charge carriers in the system. It showed that the binary mixture of Sm and Co ions can control the electrical behavior of calcium-lead hexaferrite nanomaterial. The conduction potential of the doped material may be explained based on the hopping conduction mechanism of localized charge carriers. Applications of M-type lead hexaferrites on real textile wastewater, where multiple contaminants were present are lacking in the published literature. Generally, $Ca_{0.5}Pb_{0.5-x}Sm_xCo_yFe_{12-y}O_{19}$ (x = 0.10; y = 1.00) exhibited promising photocatalytic of 87.50% for the degradation of MB dye from the aqueous solutions in the presence of solar radiations. Due to their unique electrical and photocatalytic properties, these ferrite materials were expected to be used in high-frequency devices and for textile wastewater treatment to reduce environmental pollution.

Acknowledgments

The authors are highly thankful to The Islamia University of Bahawalpur for providing financial support for this work.

References

[1] R.C. Pullar, Hexagonal ferrites: a review of the synthesis, properties and applications of hexaferrite ceramics, Prog. Mater. Sci., 57 (2012) 1191–1334.
[2] K. Zhai, N. Su, J. Sun, J. Cheng, Z. Liu, Y. Sun, Pressure effect on spin-driven multiferroicity in a Y-type hexaferrite, J. Mater. Chem. C, 7 (2019) 4173–4177.
[3] M. Elansary, M. Belaiche, C.A. Ferdi, E. Iffer, I. Bsoul, New nanosized Gd–Ho–Sm doped M-type strontium hexaferrite for water treatment application: experimental and theoretical investigations, RSC Adv., 10 (2020) 25239–25259.
[4] A.V. Timofeev, V.G. Kostishin, D.B. Makeev, D.N. Chitanov, Magnetic properties of barium hexaferrite compacted nanopowders, Tech. Phys., 64 (2019) 1484–1487.
[5] S.M. Ghahfarokhi, Z. Rostami, I. Kazeminezhad, Fabrication of $PbFe_{12}O_{19}$ nanoparticles and study of their structural, magnetic and dielectric properties, J. Magn. Magn. Mater., 399 (2016) 130–142.
[6] W. Mahmood, A. Haq, M. Anis-ur-Rehman, Electrical behavior of lead-doped Ba-hexaferrite for smart applications, Iran. J. Sci. Technol. Trans. A: Sci., 43 (2019) 1321–1325.
[7] K. Chahal, K.S. Samra, Magnetic and dielectric behavior of praseodymium substituted barium hexaferrite, J. Alloys Compd., 737 (2018) 387–391.
[8] R.S. Azis, N.N. Che Muda, J. Hassan, A.H. Shaari, I.R. Ibrahim, M.S. Mustaffa, S. Sulaiman, K.A. Matori, Y.W. Fen, Effect of ratio in ammonium nitrate on the structural, microstructural, magnetic, and AC conductivity properties of $BaFe_{12}O_{19}$, Materials, 11 (2018) 2190, doi: 10.3390/ma11112190.
[9] M.M. Barakat, D.E.-S. Bakeer, A.-H. Sakr, Structural, Magnetic properties and electron paramagnetic resonance for $BaFe_{12-x}HgxO_{19}$ hexaferrite nanoparticles prepared by co-precipitation method, J. Taibah Univ. Sci., 14 (2020) 640–652.
[10] A.A. Rodríguez-Rodríguez, M.B. Moreno-Trejo, M.J. Meléndez-Zaragoza, V. Collins-Martínez, A. López-Ortiz, E. Martínez-Guerra, M. Sánchez-Domínguez, Spinel-type ferrite nanoparticles: synthesis by the oil-in-water microemulsion reaction method and photocatalytic water-splitting evaluation, Int. J. Hydrogen Energy, 44 (2019) 12421–12429.
[11] J. Calvo-de la Rosa, M. Segarra, Optimization of the synthesis of copper ferrite nanoparticles by a polymer-assisted sol–gel method, ACS Omega, 4 (2019) 18289–18298.
[12] M. Airimioaei, C. Ciomaga, N. Apostolescu, L. Leontie, A. Iordan, L. Mitoseriu, M. Palamaru, Synthesis and functional properties of the $Ni_{1-x}Mn_xFe_2O_4$ ferrites, J. Alloys Compd., 509 (2011) 8065–8072.
[13] M. Sertkol, Y. Köseoğlu, A. Baykal, H. Kavas, M.S. Toprak, Synthesis and magnetic characterization of $Zn_{0.7}Ni_{0.3}Fe_2O_4$ nanoparticles via microwave-assisted combustion route, J. Magn. Magn. Mater., 322 (2010) 866–871.
[14] A.C.F. Costa, M.R. Morelli, R.H. Kiminami, Microstructure and magnetic properties of $Ni_{1-x}Zn_xFe_2O_4$ synthesized by combustion reaction, J. Mater. Sci., 42 (2007) 779–783.
[15] K. Jalaiah, K.C. Mouli, R. Krishnaiah, K.V. Babu, P.S. Rao, The structural, DC resistivity and magnetic properties of Zr and Co co-substituted $Ni_{0.5}Zn_{0.5}Fe_2O_4$, Heliyon, 5 (2019) e01800.
[16] L.N. Alyabyeva, V.I. Torgashev, E.S. Zhukova, D.A. Vinnik, A.S. Prokhorov, S.A. Gudkova, D.R. Góngora, T. Ivek, S. Tomić, N. Novosel, Influence of chemical substitution on broadband dielectric response of barium-lead M-type hexaferrite, New J. Phys., 21 (2019) 063016–063030.

[17] G. Kheraldeen Kara, M. Rabbani, Experimental study of methylene blue adsorption from aqueous solutions onto Fe_3O_4/NiO nano mixed oxides prepared by ultrasonic assisted co-precipitation, J. Nanostruct., 9 (2019) 287–300.
[18] M. Yousefi, S. Afghahi, M. Amini, M.B. Torbati, Sr(CeNd)$_x$Fe$_{12-2x}$O$_{19}$/polythiophene nano-particles: structral investigation, magnetic properties and photocatalyic activity, Inorg. Chem. Commun., 121 (2020) 108214, doi: 10.1016/j.inoche.2020.108214.
[19] M. Rafatullah, O. Sulaiman, R. Hashim, A. Ahmad, Adsorption of methylene blue on low-cost adsorbents: a review, J. Hazard. Mater., 177 (2010) 70–80.
[20] X. Zhang, M. Shakeel, B. Li, J. Zhang, L. Wang, Synthesis of foamed zinc oxide–silica spheres coupled with g-C_3N_4 nanosheets for visible light photocatalysis, J. Mater. Sci., 54 (2019) 13118–13134.
[21] S. Dhananasekaran, R. Palanivel, S. Pappu, Adsorption of methylene blue, bromophenol blue, and coomassie brilliant blue by α-chitin nanoparticles, J. Adv. Res., 7 (2016) 113–124.
[22] C. Arora, S. Soni, S. Sahu, J. Mittal, P. Kumar, P.K. Bajpai, Iron based metal organic framework for efficient removal of methylene blue dye from industrial waste, J. Mol. Liq., 284 (2019) 343–352.
[23] B. Kaith, J. Sharma, Sukriti, S. Sethi, T. Kaur, U. Shanker, V. Jassal, Fabrication of green device for efficient capture of toxic methylene blue from industrial effluent based on $K_2Zn_3[Fe(CN)_6]_2{\cdot}9H_2O$ nanoparticles reinforced gum xanthan-psyllium hydrogel nanocomposite, J. Chin. Adv. Mater. Soc., 4 (2016) 249–268.
[24] H.K. Choudhary, R. Kumar, A. Anupama, B. Sahoo, Effect of annealing temperature on the structural and magnetic properties of Ba-Pb-hexaferrite powders synthesized by sol–gel auto-combustion method, Ceram. Int., 44 (2018) 8877–8889.
[25] S.M. Chaudhari, P.M. Gawal, P.K. Sane, S.M. Sontakke, P.R. Nemade, Solar light-assisted photocatalytic degradation of methylene blue with Mo/TiO_2: a comparison with Cr- and Ni-doped TiO_2, Res. Chem. Intermed., 44 (2018) 3115–3134.
[26] B. Unal, M. Almessiere, Y. Slimani, A. Baykal, A. Trukhanov, I. Ercan, The conductivity and dielectric properties of neobium substituted Sr-hexaferrites, Nanomaterials, 9 (2019) 1168, doi: 10.3390/nano9081168.
[27] H.M. Khan, M. Islam, Y. Xu, M.A. Iqbal, I. Ali, M. Ishaque, M.A. Khan, Structural, magnetic, and microwave properties of NdZn-substituted $Ca_{0.5}Ba_{0.5}Fe_{12}O_{19}$ hexaferrites, J. Sol-Gel Sci. Technol., 75 (2015) 305–312.
[28] T. Jayakumar, C.R. Raja, S. Arumugam, Structural, magnetic and optical analysis of Pb^{2+}-and Ce^{3+}-doped strontium hexaferrite, J. Supercond. Novel Magn., (2020) 1–8, doi: 10.1007/s10948-020-05493-3.
[29] M.J. Iqbal, S. Farooq, Suitability of $Sr_{0.5}Ba_{0.5-x}Ce_xFe_{12-y}Ni_yO_{19}$ co-precipitated nanomaterials for inductor applications, J. Alloys Compd., 493 (2010) 595–600.
[30] A. Guerrero, M. Mirabal-García, S. Palomares-Sánchez, J. Martínez, Effect of pb on the magnetic interactions of the M-type hexaferrites, J. Magn. Magn. Mater., 399 (2016) 41–45.
[31] N. Yasmin, S. Abdulsatar, M. Hashim, M. Zahid, S.F. Gillani, A. Kalsoom, M.N. Ashiq, I. Inam, M. Safdar, M. Mirza, Structural and magnetic studies of Ce-Mn doped M-type $SrFe_{12}O_{19}$ hexagonal ferrites by sol–gel auto-combustion method, J. Magn. Magn. Mater., 473 (2019) 464–469.
[32] M.A. Darwish, A.V. Trukhanov, O.S. Senatov, A.T. Morchenko, S.A. Saafan, K.A. Astapovich, S.V. Trukhanov, E.L. Trukhanova, A.A. Pilyushkin, A.S.B. Sombra, Investigation of AC-measurements of epoxy/ferrite composites, Nanomaterials, 10 (2020) 492–508.
[33] M. Almessiere, B. Unal, Y. Slimani, A.D. Korkmaz, N. Algarou, A. Baykal, Electrical and dielectric properties of Nb^{3+} ions substituted Ba-hexaferrites, Results Phys., 14 (2019) 102468, doi: 10.1016/j.rinp.2019.102468.
[34] T. Amjad, I. Sadiq, A.B. Javaid, S. Riaz, S. Naseem, M. Nadeem, Investigation of structural, electrical, electrical polarization and dielectric properties of CTAB assisted Ni^{2+} substituted R-type nano-hexaferrites, J. Alloys Compd., 770 (2019) 1112–1118.
[35] B. Ahmad, S. Mumtaz, N. Karamat, R.S. Gohar, M.N. Ashiq, A. Shah, Synthesis, dielectric and magnetic properties of Mn-Ge substituted Co_2Y hexaferrites, J. Saudi Chem. Soc., 23 (2019) 407–416.
[36] C. Xu, A.-L. Zhang, Z. Feng, W. Lu, B. Kang, J. Zhang, J.-Y. Ge, S. Cao, Spin–orbit coupling in magnetoelectric $Ba_3(Zn_{1-x}Co_x)_2Fe_{24}O_{41}$ hexaferrites, Phys. Chem. Chem. Phys., 21 (2019) 25826–25837.
[37] Z. Zhuge, X. Liu, T. Chen, Y. Gong, C. Li, L. Niu, S. Xu, X. Xu, Z.A. Alothman, C.Q. Sun, Highly efficient photocatalytic degradation of different hazardous contaminants by $CaIn_2S_4$-$Ti_3C_2T_x$ Schottky heterojunction: an experimental and mechanism study, Chem. Eng. J., (2020) 127838, doi: 10.1016/j.cej.2020.127838.
[38] X. Liu, B. Liu, L. Li, Z. Zhuge, P. Chen, C. Li, Y. Gong, L. Niu, J. Liu, L. Lei, $Cu_2In_2ZnS_5$/Gd_2O_2S: Tb for full solar spectrum photoreduction of Cr(VI) and CO_2 from UV/Vis to near-infrared light, Appl. Catal., B, 249 (2019) 82–90.
[39] Z. Ren, X. Liu, Z. Zhuge, Y. Gong, C.Q. Sun, $MoSe_2$/ZnO/ZnSe hybrids for efficient Cr(VI) reduction under visible light irradiation, Chin. J. Catal., 41 (2020) 180–187.
[40] M. Ikram, E. Umar, A. Raza, A. Haider, S. Naz, A. Ul-Hamid, J. Haider, I. Shahzadi, J. Hassan, S. Ali, Dye degradation performance, bactericidal behavior and molecular docking analysis of Cu-doped TiO_2 nanoparticles, RSC Adv., 10 (2020) 24215–24233.
[41] B. Liu, X. Liu, J. Liu, C. Feng, Z. Li, C. Li, Y. Gong, L. Pan, S. Xu, C.Q. Sun, Efficient charge separation between UiO-66 and $ZnIn_2S_4$ flowerlike 3D microspheres for photoelectron-chemical properties, Appl. Catal., B, 226 (2018) 234–241.
[42] B. Liu, X. Liu, L. Li, Z. Zhuge, Y. Li, C. Li, Y. Gong, L. Niu, S. Xu, C.Q. Sun, $CaIn_2S_4$ decorated WS_2 hybrid for efficient Cr(VI) reduction, Appl. Surf. Sci., 484 (2019) 300–306.
[43] S.K. Tammina, B.K. Mandal, N.K. Kadiyala, Photocatalytic degradation of methylene blue dye by nonconventional synthesized SnO_2 nanoparticles, Environ. Nanotechnol. Monit. Manage., 10 (2018) 339–350.